Electrocatalysis under cover: enhanced hydrogen evolution via defective graphene-covered Pt(111)

Shih, A.J.; Arulmozhi, N.; Koper, M.T.M.

ACS Catalysis

pubs.acs.org/acscatalysis

Research Article

Electrocatalysis under Cover: Enhanced Hydrogen Evolution via Defective Graphene-Covered Pt(111)

Arthur J. Shih,*,‡ Nakkiran Arulmozhi,‡ and Marc T. M. Koper*

Cite This: *ACS Catal.* 2021, 11, 10892−10901

Read Online

ACCESS | Metrics & More | Article Recommendations | Supporting Information

ABSTRACT: The production of hydrogen via water electrolysis using renewable electricity is a promising carbon-neutral technology. In this contribution, we report insights into the hydrogen evolution reaction (HER) in H_2SO_4 on Pt(111) and graphene-covered Pt(111), in addition to the electrochemical properties of graphene overlayers. As-prepared graphene overlayers are selectively permeable to H^+ ions in the electrolyte, allowing H^+ ions into the confined layer between graphene and Pt(111) while excluding SO_4^{2-} and other anions. We demonstrate that defects in these as-prepared graphene overlayers can be generated from oxidation at high overpotentials or reduction from the production of H_2 bubbles and postulate that HER occurs locally at only Pt(111) in the proximity of defects in graphene overlayers on as-prepared G/Pt(111) electrodes, and as defects in graphene increases, more of the Pt(111) surface becomes utilized for HER. Kinetically, the addition of defective graphene overlayers can increase the geometric HER rate by up to 200%, while Tafel slopes and $[H^+]$ reaction orders remain unchanged. These results shed kinetic insight into the nature of graphene overlayers and their effect on HER catalysis and also demonstrate the promise of confinement modifications in designing catalysts with properties closer to achieving optimum rates.

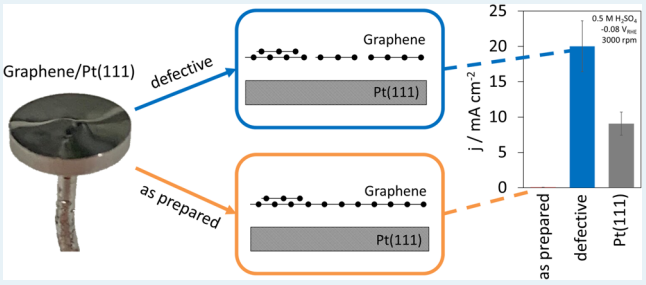

KEYWORDS: *graphene, Pt(111), confinement, hydrogen evolution reaction, intercalation, transport limitations, defect engineering*

1. INTRODUCTION

With the rise and demand for green energy stemming from climate change, fundamental understanding and ultimate deployment of carbon-neutral or carbon-negative technologies are in pressing need. One promising method for the production of non-fossil-fuel-based energy and products involves utilizing electricity produced from renewable resources (solar, wind, etc.) to produce hydrogen fuel from water over an electrocatalyst. Computational and experimental studies on a variety of model catalytic surfaces have led to design rules where the reaction rate of catalysts is found to correlate with descriptors such as the binding energy of intermediates. These correlations, called volcano plots, suggest that the optimal catalyst exhibits moderate binding energies of the relevant intermediates that are neither too strong nor too weak.[1−3] Several computational studies have demonstrated that reaction rates faster than the optimum of the volcano are limited by scaling relations between different intermediates.[4,5] In an effort to understand these scaling relations and further optimize catalysis, researchers are turning their focus toward a variety of catalyst modification strategies.[5] In this work, we utilize one of these modification strategies—confinement—by covering Pt(111) with graphene overlayers and studying its effect on the hydrogen evolution reaction (HER).

The effect of overlayer confinement on single crystals for catalysis has previously been studied for low-pressure CO oxidation. Zhang et al. observed that a hexagonal boron nitride (h-BN) confining layer over Pt(111) increases CO oxidation reaction rates at temperatures lower than 225 °C and decreases CO oxidation rates at temperatures higher than 225 °C (8 Torr CO, 4 Torr O_2, 200−300 °C).[6] Yao et al. observed that graphene-covered Pt(111) decreases CO oxidation reaction rates at temperatures higher than 250 °C and increases CO oxidation rates at temperatures lower than 250 °C (20 Torr CO, 10 Torr O_2, 200−400 °C).[7] CO oxidation rates were also observed to increase on h-boron-nitride-confined Pt nanoparticles.[8] These results suggest that confining overlayers may have a significant effect on CO oxidation rates at low temperatures where rates are limited by kinetics and transition to mass-transfer limited rates with increasing temperature.[9−11] It has also been demonstrated that CO_2 reduction selectivity may be tuned when catalytically active surfaces are confined by

Received: May 12, 2021
Revised: August 5, 2021
Published: August 17, 2021

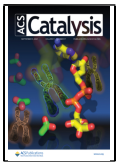

flat organic molecules.[12−14] Specifically, for hydrogen evolution, HER rates are enhanced when Pt(111) is covered by flat caffeine molecules,[15] and electrode stability is improved when Pt is confined by SiO_x nanomembranes.[16−18]

The effect of overlayer confinement on single crystals has also been studied with density functional theory (DFT) calculations. The results of DFT calculations reported by Gao et al. exhibit no significant changes in the graphene electronic structure between free-standing graphene and graphene on Pt(111), indicating weak interaction between graphene and Pt(111).[19] Furthermore, Li et al. demonstrated that the Gibbs free energy of adsorption decreases slightly for a variety of adsorbates (H, C, N, O, S, O_2, OH, NO, CO, among others) on several metal surfaces including Pt(111).[20] Zhou et al.[21] also computed a decrease in Gibbs free energy of adsorption of H on metal (111) surfaces after the addition of a graphene overlayer. In addition, Trasatti et al. and Greeley et al. demonstrated that the HER rate follows a volcano-type plot as a function of the computed Gibbs free energy of absorption of H for a number of metal surfaces.[2,3,22,23] Since Pt(111) lies on the strong binding leg of the volcano,[3] if we combine this observation with the predicted shift in the Gibbs free energy of H toward weaker binding,[20,21] the prediction is that a Pt(111) surface covered by a graphene overlayer should be a better catalyst than unmodified Pt(111).

Fu et al. experimentally synthesized and characterized graphene overlayers on Pt(111) using cyclic voltammetry (CV) and demonstrated that the HER onset overpotential is about ∼0.1 V more negative on G/Pt(111) than on Pt(111) in H_2SO_4, $HClO_4$, HCl, and NaOH, indicating a decrease in the HER rates in the presence a graphene overlayer on Pt(111), seemingly in contradiction with the predictions by DFT. We demonstrate in this contribution that this contradiction and low HER rates on G/Pt(111) are due to HER transport limitations through graphene overlayers. Fu et al. also demonstrated that graphene overlayers selectively allow H adsorption through H^+ transfer while preventing anions (SO_4^{2-}, Cl^-, OH^-, ClO_4^-) from adsorbing to Pt(111).[24] This selectivity was also later demonstrated by Baby et al. on G/Pt(111)[25,26] and by Hu et al. on G/Ni and G/Cu.[27] It was also shown by Fu et al. that multilayer graphene suppresses both H adsorption and HER.[24,27]

Defect-free graphene has been demonstrated to tunnel H^+ ions at rates 3 orders of magnitude faster than gases (He, H_2, N_2, O_2, etc.).[28−31] Furthermore, the introduction of local curvature (e.g., ripples, folds, wrinkles, etc.) to defect-free graphene has been postulated to increase the permeation rate of H_2.[32] In reality, however, when graphene is grown via chemical vapor deposition (CVD) on single-crystal metal surfaces, defects at both graphene domain boundaries and within the graphene domain are observed using atomic-resolution scanning tunneling microscopy (STM).[19,33,34] Studies have also observed convex features on the order of 10 nm on graphene overlayers during hydrogen evolution with atomic force microscopy (AFM) and scanning tunneling microscopy (STM) and that the density of these convex features is ten times more dense on pristine graphene than on defective graphene; these convex features are attributed to trapped H_2 bubbles below graphene.[35,36] Therefore, it is still unclear how graphene modulates the reactivity of Pt(111), and how graphene affects the transport of reactants and products to and from Pt(111).

In this study, we report the effect of different electrochemical pretreatments on kinetic and physical properties of G/Pt(111) and demonstrate that defective graphene is necessary to overcome inherent transport limitations of H^+ and H_2 through graphene overlayers. With these transport limitations out of the way, defective G/Pt(111) turns out to be indeed a better catalyst for HER than unmodified Pt(111).

2. EXPERIMENTS AND METHODS

2.1. Borosilicate Cell Cleaning Preparation. In-house borosilicate cells and all other glassware to be used in the electrolyte preparation were cleaned using a procedure outlined in Arulmozhi et al.[37] In summary, glassware was soaked in a 0.5 M H_2SO_4 solution (Sigma-Aldrich, 95.0−97.0%) containing 1 g L^{-1} $KMnO_4$ (Sigma-Aldrich, ≥99.0%) for at least 48 h at 23 °C. The glassware was then removed from the solution, rinsed 3 times with ultra-high-purity (UHP) water (Merck Milli-Q IQ 7000, <5 ppb total organic content (TOC), 18.2 MΩ·cm at 25 °C) before submersion in piranha solution (∼1 M H_2SO_4 (Sigma-Aldrich, 95.0−97.0%) and ∼6% H_2O_2 (Merck KGaA, 35%)) at 23 °C to dissolve traces of $KMnO_4$ and MnO_2 for at least 30 min. The glassware was then rinsed 3 times with UHP water and an additional 10 times with boiling UHP water. All plastics to be in contact with the electrolyte or the electrochemical cell were placed in a clean borosilicate beaker, sonicated for 30 min in UHP water at 23 °C, and then washed 10 times with boiling UHP water. Impurities reported by vendors for all chemicals used during the cleaning process are listed in Table S01.

2.2. Electrolyte, Electrode, and Reference-Electrode Preparation. The sulfuric acid (H_2SO_4) electrolyte between 0.005 and 0.5 M was prepared by diluting H_2SO_4 (Sigma-Aldrich, TraceSELECT Ultra, ≥95%) with UHP water. A pH meter (SI Analytics Lab 855) equipped with a pH electrode (SI Analytics, BlueLine 14 pH) and pH buffer standards (Hach, Certified Buffer Standard Solution, pH 4.005 and pH 1.679 at 25 °C) were used to measure and confirm the electrolyte molarity after the completion of electrochemical experiments to circumvent electrolyte contamination. The electrolyte that had been in contact with a pH probe was never used for electrochemical measurements. A parity plot between the expected H_2SO_4 molarity calculated from the dilution equation and measured H_2SO_4 molarity using the pH meter confirms parity between the two methods (Supporting Information, Section 3.1). Errors (two times the standard deviation to cover ∼95% of the spread) in the pH were calculated to be ∼17% using both error propagation (Supporting Information, Section 4) and repeat measurements. Impurities reported by vendors for all chemicals used for electrolytes are listed in Tables S02 and S03.

A Pt(111) disk (Surface Preparation Laboratory (SPL), 6, 7, or 10 mm diameter disk) was flame-annealed at the tip of the blue flame from two butane torches (Toolcraft MT-770S with FlameClassics Universal Gas Lighter Refill) for at least 3 min prior to transfer to a cooling cell saturated with flowing 1:4 v/v H_2/Ar to cool for 5−10 min.[38,39] After cooling to room temperature, the Pt(111) was protected with a bead of water saturated with the cooling gas, quickly transferred in ambient air to the electrochemical cell (typically ∼10 to 20 s), and deaerated for 5 min in flowing Ar in the volume above the electrolyte. After confirming a quality Pt(111) crystal via cyclic voltammetry (Supporting Information, Section 2.2), graphene was grown in an induction cell via chemical vapor deposition

https://doi.org/10.1021/acscatal.1c02145
ACS Catal. 2021, 11, 10892−10901

(CVD) in a mixture of ethylene, hydrogen, and argon using the procedure reported in Fu et al.[24] We note that it has been demonstrated that etching of the graphene overlayers by H_2 also occurs during CVD, with consequences on the morphology of the grown graphene.[40]

The counter electrode used is a Pt sheet whose submerged surface area is >2 times the surface area of the working electrode to avoid limiting currents due to geometric constraints.[41] The counter electrode was cleaned via flame annealing at the tip of the blue flame from two butane torches until no orange tint (indicative of sodium contamination) in the flame is observed, then allowed to cool to room temperature in ambient air prior to contact with the electrolyte. The working electrode was brought into contact with the aqueous H_2SO_4 electrolyte at 0.1 V_{RHE} via a hanging-meniscus configuration.[42] Two reference electrodes were used in this study: a Hydroflex (Gaskatel GmbH) reversible hydrogen electrode (RHE) and a custom reversible hydrogen electrode (RHE) that consists of hydrogen gas bubbling through a platinum wire in contact with the solution. Both the Hydroflex and custom RHE were separated from the main electrolyte via a Luggin capillary.[43] Impurities reported by vendors for all chemicals used during the electrode preparation process are listed in Table S02.

2.3. Electrode Characterization Using SEM. Pt(111) and G/Pt(111) were imaged using a Thermo Scientific Apreo S scanning electron microscope (SEM). Pt(111) surfaces were collected with a 15.00 kV and 0.40 nA electron beam at 150, 1000, and 5000 magnification. G/Pt(111) surfaces were collected with a 15.00 kV and 0.025 to 0.40 nA electron beam at 150, 1000, 5000, 30 000, and 60 000 magnification. To avoid bias in acquisition and analysis, imaging locations were determined by generating five random pairs of angles between 0 and 360° and radii with the constraint that no two points can be 0.5 mm from each other.[44,45]

2.4. Electrode Characterization Using Cyclic Voltammetry (CV). The electrolyte was first saturated by flowing 100 to 200 sccm Ar (Linde, 6.0 Scientific Grade 99.9999%) for 30 min through two apertures: one through the electrolyte and another into the chamber above the electrolyte. When saturated, argon bubbling through the electrolyte is shut off to ensure an unperturbed electrolyte surface as argon continues to saturate the chamber above the electrolyte. The working electrode potential was set to 0.1 V_{RHE} and a hanging-meniscus contact between the working electrode and the electrolyte was carefully formed. When the current reached steady state (typically between 10 s and 4 min), six cyclic voltammograms (CVs) were collected between 0.1 and 1.0 V_{RHE} with scan rates of 50 mV s^{-1}. After completion, the potential was set to 0.1 V_{RHE} prior to breaking the meniscus between the electrode and electrolyte solution. We proceed to further measurements if the CVs are characteristic of quality Pt(111) or G/Pt(111).[24,37]

2.5. Steady-State Kinetic Measurements (Rates, Tafel Slopes, Reaction Orders) Using Chronoamperometry (CA). Steady-state kinetic measurements were collected in Ar-saturated (Linde, 6.0 Scientific Grade 99.9999%) and H_2-saturated (Linde, 5.0 Detector Grade 99.999%) H_2SO_4. Once saturated with Ar or H_2, the potential is set to 0.1 V_{RHE} and a hanging-meniscus contact between the electrode and electrolyte is carefully formed. Steady-state HER rates between potentials of 0.0 and −0.1 V_{RHE} were collected with periodic repeats at −0.08 and −0.02 V_{RHE} to rule out systematic errors (Figure S01) and to ensure that the continual production of H_2 does not significantly affect the HER rate throughout the experiment. Back-of-the-envelope calculations using the maximum HER rate measured (0.5 M H_2SO_4 at −0.1 V_{RHE}) indicate that only 1/660 of the saturation limit of H_2 would be reached during the time frame of the experiment if all H_2 produced is dissolved in the electrolyte (Supporting Information, Section 1.2). All currents and rates reported in this study were normalized to the geometric area of the electrode disk and corrected 100% for internal resistance (Supporting Information, Section 3.2). Tafel slopes and $[H^+]$ orders were computed using eqs 1,2. $[H^+]$ orders were reported on the RHE scale. Supporting Information, Section 3.4 discusses the influence of using a RHE and normal hydrogen electrode (NHE) scales in analyzing reaction order data and presents our results on bare Pt(111). All reported errors are 2 times the standard deviation, which cover approximately 95% of scattering in the data. If repeats were difficult or too time consuming, error propagation[46] was used to estimate the error (Supporting Information, Section 4).

$$\text{Tafel slope} = \frac{d(E)}{d(\log(j))} \tag{1}$$

$$[H^+]\ \text{order} = \frac{d(\log(j))}{d(\log[H^+])} \tag{2}$$

2.6. Treatments and HER Testing Protocols. Two different treatments (Table 1) were employed to study the effect of different defect generation pretreatments on graphene overlayers: only cathodic currents (as-prepared) and one block of 250 oxidation−reduction cycles followed by cathodic currents (EC-treated). The as-prepared G/Pt(111) involved only H_2 generation during cathodic polarization, while the EC-treated G/Pt(111) involved one oxidation−reduction cycling block followed by H_2 generation. Both of these treatments were used to study the long-term (>15 h HER) implications of HER generation on the G/Pt(111) electrode where the permeability of graphene was probed with CVs, surface structures with SEM, and HER kinetics (rates, Tafel slopes, and reaction orders) with chronoamperometry.

Table 1. Summary of the Three Different Treatments Subjected on G/Pt(111) Electrodes

defect generation method	description
as-prepared G/Pt(111)	Only HER between −0.1 and 0.0 V_{RHE}
EC-treated G/Pt(111)	250 cycles between 0.1 and 1.2 V_{RHE} at 500 mV s^{-1} in 0.005 M H_2SO_4 prior to HER between −0.1 and 0.0 V_{RHE}

3. RESULTS AND DISCUSSION

3.1. Benchmarking HER for Pt(111) in H_2SO_4 with the Literature. CVs and HER rates measured on Pt(111) in H_2SO_4 quantitatively match the literature. The shape of the Pt(111) CV in 0.005−0.5 M H_2SO_4 in addition to the potential and intensity of the H^+ adsorption feature and sharp sulfate peak match those reported in the literature (Supporting Information, Section 2.2).[47] HER rates reported on Pt(111) in inert-gas-saturated 0.5 M H_2SO_4 by Kita et al. and Gómez et al.[48,49] (Figure S05) and H_2-saturated 0.5 M H_2SO_4 by

https://doi.org/10.1021/acscatal.1c02145
ACS Catal. 2021, 11, 10892−10901

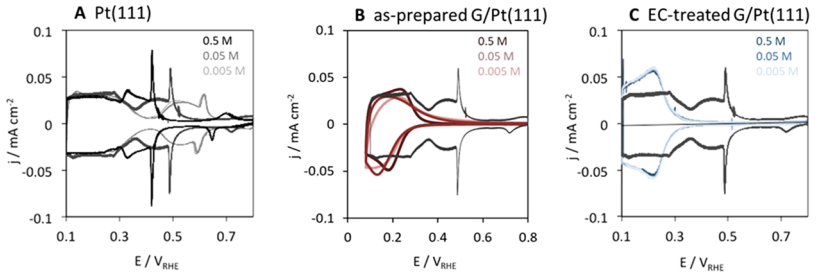

Figure 1. Cyclic voltammograms of (A) Pt(111), (B) as-prepared G/Pt(111), and (C) EC-treated G/Pt(111) in Ar-saturated 0.005, 0.05, and 0.5 M H_2SO_4 at scan rates of 50 mV s^{-1} at 23 °C. Each CV includes the first 5 cycles.

Marković et al.[50] (Figure S06) are also indistinguishable from our measurements within error. In addition, the independence of steady-state HER rates from rotation (0 and 3000 rpm), electrolyte concentration (0.005−0.5 M H_2SO_4), and potential (0 to −0.1 V_{RHE}) on Pt(111) was also validated[48] (Figures S07 to S09). The error of our steady-state HER rates measured at 3000 rpm (calculated as two times the standard deviation to contain ∼95% of the data) from repeat measurements was determined to be ∼18%.

3.2. Graphene Overlayers are Selective to H^+ but not to Anions. CVs of as-prepared G/Pt(111) in Ar-saturated 0.005, 0.05, and 0.5 M H_2SO_4 exhibit asymmetric irreversibility in the H^+ underpotential deposition (H_{UPD}) region between 0.1 and 0.4 V_{RHE} where decreasing concentrations from 0.5 to 0.005 M H_2SO_4 lead to increased irreversibility (Figure 1B). After EC treatment, this H_{UPD} region becomes more symmetric and reversible (Figure 1C). Furthermore, the CVs are independent of the H_2SO_4 concentration (Figure 1C) and our G/Pt(111) CVs quantitatively match with CVs reported by Fu et al.[24] Several phenomena can be deduced from these CVs, the first of which is that graphene overlayers selectively allow H^+ adsorption/desorption while excluding SO_4^{2-} and other anions. Second, as-prepared graphene overlayers exhibit resistance toward H^+ transport in the H_{UPD} region, exhibited by an asymmetric CV response that becomes more irreversible with lower $[H^+]$ concentration. Third, EC treatment drastically reduces irreversibility in the H_{UPD} region, indicating that the resistance against H^+ adsorption/desorption in as-prepared G/Pt(111) is no longer limiting, due to the creation of defects conducive toward facile H^+ transport across graphene overlayers, as demonstrated with electrochemical impedance spectroscopy by Arulmozhi et al.[51]

3.3. Defective Graphene Increases Permeation to SO_4^{2-} and Exhibits Equal or Higher HER Rates Compared to Pt(111). We observe an increase in HER rates with reaction time on both as-prepared and EC-treated G/Pt(111) (Figure 2A,B) in 0.005 M H_2SO_4, indicating that both EC treatment and HER treatment are capable of increasing the HER rate by increasing the rate of H^+ and H_2 transport across graphene via the formation of defects within the graphene. It has been demonstrated that HER treatment is able to induce structural changes and defects onto unsupported multilayer graphene.[52] Rotating disk voltammetry studies indicate that currents measured on G/Pt(111) after 10+ h of HER increase with the rotation rate but remain constant for rotation rates higher than 1000 rpm (Figure S22). Because the change in currents does not follow Koutecky−Levich[53] and we visibly see the removal of bubbles, we deduce that rotation does not improve Fickian diffusion but rather prevents H_2 bubbles from accumulating on the electrode and

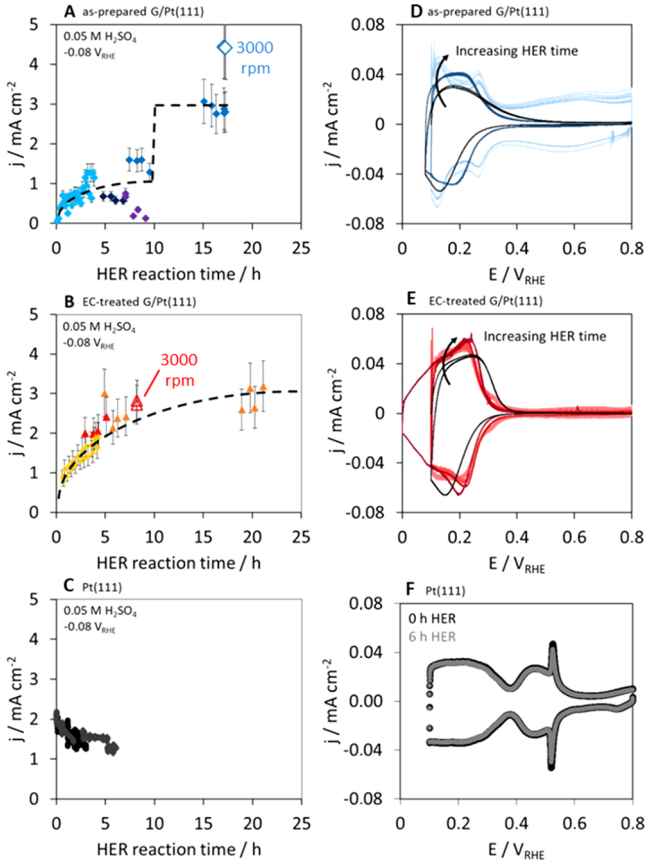

Figure 2. Geometric current densities measured in 0.05 M H_2SO_4 at −0.08 V_{RHE}. Solid and hollow shapes are currents collected at 0 rpm and 3000 rpm, respectively. HER rates measured at steady-state chronoamperometry (CA) at −0.08 V_{RHE} in 0.05 M H_2SO_4 on as-prepared G/Pt(111) (A), EC-treated G/Pt(111) (B), and Pt(111) (C). Corresponding CVs on as-prepared G/Pt(111) (D), EC-treated G/Pt(111) (E), and Pt(111) (F) are also plotted to demonstrate changes in the CV with increasing HER reaction time. Each CV includes the first 5 cycles.

fouling the currents. In other words, kinetically limited currents (i.e., intrinsic HER rates) are achieved by removing bubbles from the surface by rotation at >1000 rpm and increasing transport rates across graphene overlayers via the introduction of defects in the graphene. All currents used to measure reaction kinetics (HER rates, Tafel slopes, and $[H^+]$ orders) will be reported at 3000 rpm, unless otherwise stated, in the remainder of this paper.

A control experiment on Pt(111) demonstrates that the HER rates decrease by ∼30% over the course of 6 h (Figure 2C) in Ar-saturated 0.05 M H_2SO_4 at 0 rpm while maintaining

https://doi.org/10.1021/acscatal.1c02145
ACS Catal. 2021, 11, 10892−10901

its Pt(111) structure as indicated by its CV (Figure 2F) collected at 0 and 6 h of HER. This demonstrates that the Pt(111) surface retains its long-range (111) structure and that the decrease is likely due to fouling of the active surface from H_2 bubbles, since breaking and reforming the meniscus resulted in HER rates equal to that measured at 0 h of HER.

With increasing HER reaction time, changes in both the H_{UPD} region (0.1 to 0.4 V_{RHE}) and anion-adsorption region (0.4 to 0.8 V_{RHE}) occur (Figure 2D,E). On as-prepared G/Pt(111), HER rates initially increase but remain at values lower than Pt(111) until a sudden increase in the HER rate to values exceeding that of Pt(111) occurs after ~10 h of HER (Figure 2A) in 0.05 M H_2SO_4. This characteristic sudden jump in HER rates occurs at the same time a sudden increase in the anion-adsorption charge per Pt occurs in the CV (Figure 2D) and indicates that a large number of anions are now able to perform charge-transfer processes with the electrode. We speculate that may be due to the formation of a porous capacitive film (similar to the results published by Labrador et al.[16] on a capacitive silicon oxide nanomembrane), there is electrochemical roughening of the Pt below the graphene and/or large rips large enough for H_2O and SO_4^{2-} ions to access the Pt surface. In particular, the appearance of Pt(110) and Pt(100) peaks in the H_{UPD} region of the CV (Figure 2D) suggests that the underlying Pt(111) has been electrochemically roughened, and this may be the most important reason for the higher HER rate under these conditions.[54] However, if we electrochemically pretreat G/Pt(111) prior to HER, this sudden increase in anion capacity associated with apparent roughening is absent, but the HER rate is still higher than in the absence of graphene. The nature of this sudden increase in current and anion-adsorption capacity will be discussed later when we discuss the SEM imaging.

The H_{UPD} feature in the presence of graphene shows two major differences with respect to the unmodified Pt(111): it has shifted to a more negative potential, suggesting a weaker binding of adsorbed H to G/Pt(111) in this potential window, and the feature is sharper than for the unmodified Pt(111), suggesting that the lateral interactions between the adsorbed H are less repulsive.[55,56] An increase in the defect density only results in a shift from an asymmetric H_{UPD} to a symmetric H_{UPD} and does not result in any major changes in the shape of the H_{UPD} feature. We do not have evidence to claim whether the edge of the graphene is saturated with the hydrogen atoms.

3.4. Electrochemical Pretreatment on the G/Pt(111) Results in Different Modes of Defect Generation during HER. The anionic charge per surface Pt atom (mol_{e-} mol_{Pt}^{-1}) is calculated by integrating the anion-adsorption region in CVs between 0.4 and 0.8 V_{RHE} using eq 3 and then plotted versus the HER reaction time (Figure 3A). F is Faraday's constant, i is the current, A is the geometric area of the electrode, N_A is Avogadro's Number, and $\rho_{Pt(111)}$ is the surface Pt density of Pt(111) (1.503×10^{15} atoms cm^{-2}).[57−60] This anionic charge per Pt gives us a quantitative measure of the permeability of the graphene, specifically the number of defects large enough for sulfate ions (HSO_4^-, SO_4^{2-}) to pass through graphene overlayers and adsorb onto the underlying Pt(111). For defects smaller than sulfate ions, impedance spectroscopy and in-situ Raman spectroscopy have been used to probe the permeability of H^+ through graphene overlayers; Arulmozhi et al. observed increases in the permeability of graphene toward H^+ with increased EC treatment.[51] The best-fit linear slope of anionic charge per Pt vs reaction time is taken as the defect generation

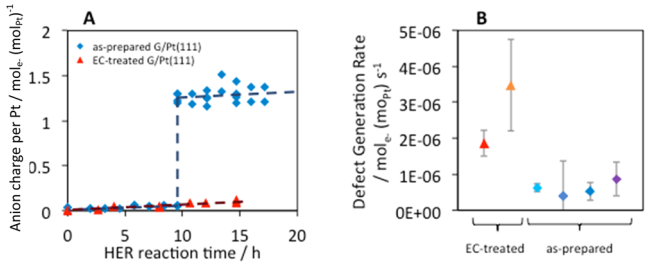

Figure 3. (A) Charge per Pt (mol_{e^-} mol_{Pt}^{-1}) of the anion-adsorption region in the CV between 0.4 and 0.8 V_{RHE}. (B) Defect generation rate measured from the slope of the anion charge per Pt versus time for pretreated and non-pre-treated G/Pt(111). Two EC-treated G/Pt(111) (red and orange triangles) and four as-prepared G/Pt(111) (blue and purple diamonds) were tested and plotted in (B).

rate with units of mol_{e-} mol_{Pt} s^{-1} (eq 4). Detailed analysis and calculations can be found in the Supporting Information, Sections 3.9 and 3.10.

On as-prepared G/Pt(111), we observe a gradual increase in anionic charge per Pt from 0 to ~10 h after which the as-prepared G/Pt(111) electrode exhibits a sudden increase in anionic charge per Pt (Figures 2D and 3A). In contrast, EC-treated G/Pt(111) exhibits only a gradual increase in anionic charge per Pt throughout the entire 15 h HER reaction time span (Figures 2E and 3A). Comparing the defect generation rate on EC-treated and as-prepared G/Pt(111), the EC-treated G/Pt(111)-exhibited defect generation rates are 2−8 times faster than on as-prepared G/Pt(111). This indicates that EC treatment (250 cycles between 0.1 and 1.2 V_{RHE} at 500 mV s^{-1} in 0.005 M H_2SO_4 at 23 °C) likely primes the graphene overlayers in such a way that results in faster defect generation. Arulmozhi et al.[51] demonstrated that EC treatment induces point defects by using Au electrodeposition[61] without inducing any long-range roughening of the underlying Pt(111) below graphene. In the absence of EC treatment, these point defects are absent, resulting in an initially lower density of defects. Taken together, we envision that EC treatment may increase the number of point defects within graphene domains or functionalized graphene with O atoms, ultimately enabling these defects to grow faster with increasing HER reaction time, relative to as-prepared G/Pt(111). Thus, our interpretation of Figure 3 is that the apparent faster increase in the defect generation rate on EC-treated G/Pt(111) is likely due to differences in the initial density of point defects on the G/Pt(111), which is undetectable with anion adsorption.

$$f = \frac{\mathrm{mol_{e^-}}}{\mathrm{mol_{Pt(111)}}} = \frac{\frac{1}{F}\int i \ \mathrm{d}t}{\frac{\rho_{Pt(111)}A}{N_A}} \tag{3}$$

$$r_{\text{defect generation}} = \frac{df_{\text{anion}}}{dt} \tag{4}$$

As discussed earlier, we also observe a sudden order-of-magnitude increase in anionic charge per Pt on as-prepared G/Pt(111) and a HER reaction time of ~10 h (Figure 2A,D). Four independent repeats were performed to test this unusual occurrence and the order-of-magnitude increase in the anion charge per Pt was observed for each at ~10 h of HER (Figure S19). In an effort to understand the cause of this occurrence, we compare the surface morphology using SEM of graphene overlayers before and after the sudden order-of-magnitude

https://doi.org/10.1021/acscatal.1c02145
ACS Catal. 2021, 11, 10892−10901

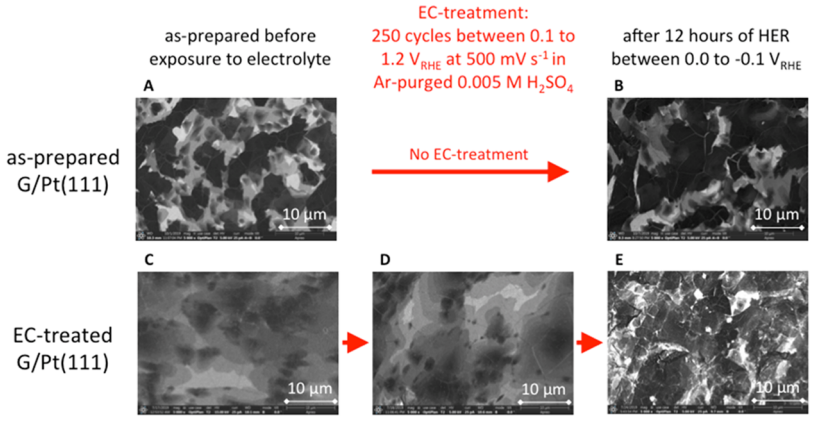

Figure 4. Representative SEM images of as-prepared G/Pt(111) before (A) and after (B) HER. Representative SEM images of as-prepared G/Pt(111) before (C), after EC treatment (D), and after HER (E).

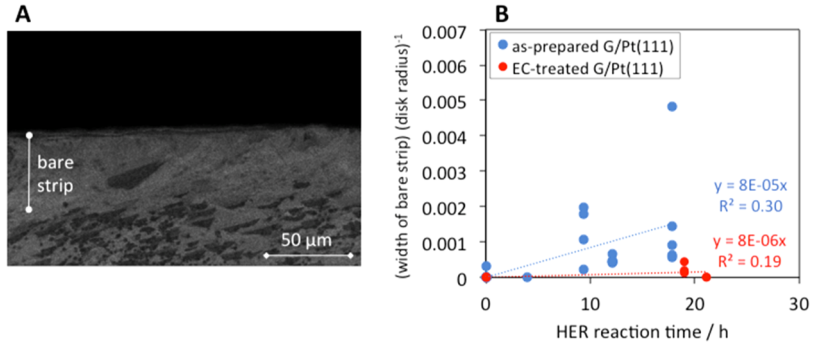

Figure 5. (A) Representative SEM image of the delaminated edge of an as-prepared G/Pt(111) after 10 h HER. (B) Fractional width of delaminated areas versus HER reaction time for as-prepared G/Pt(111) (blue circles) and EC-treated G/Pt(111) (red circles).

increase in anionic charge per Pt. We observe no qualitatively significant differences in the graphene overlayers at the center away from the edge of the as-prepared G/Pt(111) disk compared to the images taken before HER (Figure 4) but observe large cracks in the graphene (Figure S28) and bare regions (Figure 5A) along the perimeter of the as-prepared G/Pt(111) disk. We postulate that these physical changes to the graphene may be due to delamination from H_2 bubbles[35,62,63] and/or cracks due to strain on the graphene overlayer from H_2 bubbles,[64,65] which indicates that EC pretreatment possibly avoids these drastic cracks and delamination by introducing distributed defect pathways for H_2 bubbles to transport through the graphene throughout the entire electrode surface.

In contrast, SEM images of EC-treated G/Pt(111) exhibit no significant differences in graphene overlayers before and after the first electrochemical cycling pretreatment (250 cycles between 0.1 and 1.2 V_{RHE} at 500 mV s^{-1} in 0.005 M H_2SO_4) on the entire G/Pt(111) disk (both the edge and center) (Figure 4C,D). However, after 10 h of HER, SEM images of EC-treated G/Pt(111) exhibit visual cracking of graphene overlayers throughout the entire disk (Figure 4E). An analysis of images collected at 5 random locations on the disk demonstrated that we do not observe significant changes in the fraction of exposed graphene monolayers on pretreated G/Pt(111) throughout HER (Supporting Information, Section 6.2). Bare regions along the perimeter of the disk were also observed and were quantitatively lower than those observed on as-prepared G/Pt(111) after 10 h of HER (Figure 5B). Since CVs on EC-treated G/Pt(111) after 10 h of HER indicate that anion adsorption is still largely prohibited (Figure 3A), we deduce from the aforementioned CVs and SEM images that generating H_2 after EC pretreatment retains the overall structure of the full graphene monolayer immediately above the Pt(111) but cracks bi-, tri-, and higher graphene overlayers throughout the entirety of the G/Pt(111) disk. These results are consistent with DFT predictions by Ferrighi et al., where they predicted that delamination of graphene from Pt(111) is unfavorable, even in the presence of water at defects.[66] It is also possible that bonding between defective graphene may be another reason why we do not observe graphene flakes delaminating from the Pt(111).

Taken together, as illustrated in Figure 6, we propose that H^+ and H_2 transport across graphene overlayers occurs at defects scattered throughout the graphene overlayer. EC treatment increases the defect density on graphene, as evidenced by the shift from an asymmetrical H_{UPD} region to

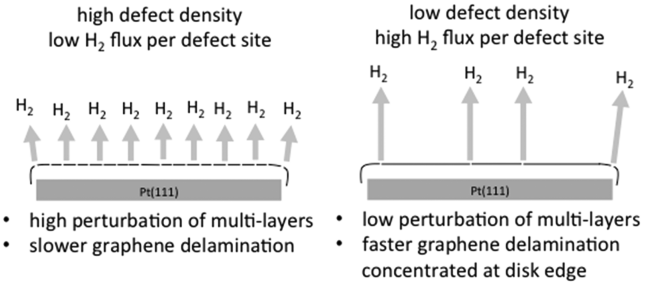

Figure 6. Proposed defect generation scheme that captures evidence from SEM, CVs, and HER rates.

https://doi.org/10.1021/acscatal.1c02145
ACS Catal. 2021, 11, 10892−10901

a symmetrical H_{UPD} region in the CV. Without EC treatment, the defect density remains so low that H^+ and H_2 transport are severely limited, likely resulting in increased rates of H_2 transport per defect site and ultimately leading to ripped overlayers and a higher concentration of delamination and/or rips at the edge of the electrode disk. Back-of-the-envelope calculations also demonstrate that H^+ tunneling through graphene is about 3 orders of magnitude slower than H^+ transport through defects in the graphene (Supporting Information, Section 1.3).

3.5. HER on As-Prepared G/Pt(111) is Initially Limited by H^+ Transport Across Graphene Overlayers. Irrespective of the mode of defect generation or the types of defects formed, after ∼10 h of HER reaction time, HER rates stabilize on both EC-treated and as-prepared G/Pt(111). Tafel plots collected in 0.005, 0.05, and 0.5 M H_2SO_4 on both Pt(111) and G/Pt(111) result in indistinguishable Tafel slopes at overpotentials between −0.06 and −0.10 V_{RHE} (Table 2). This overpotential range was chosen since it avoids the potential (>−0.06 V_{RHE}) where the HOR back reaction current is more than 1% of the total current as predicted by the Butler−Volmer equation[67,68] (Supporting Information, Section 3.3) and somewhat avoids potentials (>−0.10 V_{RHE}) where HER rates are masked by H_2 bubbles. This can be also observed when we plot the Tafel slope as a function of the overpotential (Figure S16). Furthermore, HER rates in Ar-saturated and H_2-saturated H_2SO_4 are indistinguishable within error between the potential range of −0.06 and −0.10 V_{RHE}; this demonstrates that the bulk concentration of the dissolved product (H_2) does not significantly increase the parasitic HOR current.

Table 2. Kinetic Parameters (Tafel Slopes and $[H^+]$ Orders) on Pt(111) and G/Pt(111) with Defective Graphene (>10 h HER)

electrode	Tafel slope/mV dec^{-1}	$[H^+]$ order
Pt(111)	130 ± 20	0.69 ± 0.08
as-prepared G/Pt(111), 0 h HER	∞[a]	−0.04 ± 0.13
as-prepared G/Pt(111), >10 h HER	150 ± 28	0.81 ± 0.06
EC-treated G/Pt(111), >10 h HER	156 ± 42	0.86 ± 0.06

[a]Because HER rates were collected using chronoamperometry at potentials between 0.00 and −0.10 V_{RHE} for the first 80 min when the rates were not stable and graphene was dynamically changing (Figure S02), Tafel slopes from 3 repeats were calculated to be −152, −114, and 478 between potentials of −0.07 and −0.10 V_{RHE}.

HER rates measured at −0.08 V_{RHE} also result in indistinguishable $[H^+]$ orders between Pt(111) on both EC-treated and as-prepared G/Pt(111) after ∼10 h of HER reaction time (Figure 7). From rate laws derived using Volmer, Heyrovský, and Tafel steps as rate limiting at H coverages of 0 and 1 (Supporting Information, Section 3.6),[69] our measured kinetic parameters are consistent with either a Volmer rate-limiting step (RLS) at low H coverage or a Heyrovský RLS at high (saturated) H coverage (Table 2). Though we are unable to isolate the precise RLS, we narrow down all possible scenarios to three possibilities: (1) The RLS between does not change, (2) The RLS shifts from Volmer to Heyrovský or Heyrovský to Volmer, and (3) The mechanism undergoes a process not considered in our rate law derivations.

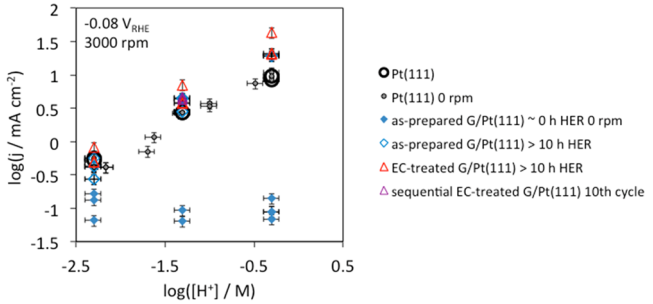

Figure 7. $[H^+]$ order plots (log of the HER rate plotted versus log of the $[H^+]$ concentration) at −0.08 V_{RHE} on Pt(111) at 3000 rpm (hollow black circles), Pt(111) at 0 rpm (filled gray circles), as-prepared G/Pt(111) at 0 rpm (filled blue diamonds), as-prepared G/Pt(111) after 10 h of HER at 3000 rpm (hollow blue diamonds), EC-treated G/Pt(111) after 10 h of HER at 3000 rpm (hollow red triangles), and sequential EC-treated G/Pt(111) after the 10th cycle at 3000 rpm (hollow purple triangle, Figure S17).

On as-prepared G/Pt(111), we measure identical currents (collected at −0.08 V_{RHE} within the first 20 min) across the 0.005−0.5 M H_2SO_4 range (solid blue diamonds, Figure 7) corresponding to a $[H^+]$ order of −0.04 ± 0.13. With increasing HER reaction time, HER rates increase such that the $[H^+]$ order also increases from −0.04 ± 0.13 to 0.81 ± 0.06. The $[H^+]$ order of ∼0.0 is a kinetic indication that the H^+ concentration does not affect HER rates on as-prepared G/Pt(111). We infer from this that the $[H^+]$ order on as-prepared G/Pt(111) is likely due to additional factors, possibly the effect of multilayers or the effect of solvation surrounding defect centers on the graphene.[70−72] Moreover, the increase in $[H^+]$ order from ∼0.0 to ∼0.8 is presumed to be due to an increase in graphene defects conducive toward increasing H^+ transport rates across the graphene overlayers, consequently shifting the limiting step from H^+ transport across graphene to kinetic catalytic surface processes.

Comparing the experimentally measured HER rate (0.1−10 mA $cm_{geometric}^{-2}$) with the tunneling rate of unsolvated protons through pristine graphene (∼0.4 mA $cm_{geometric}^{-2}$) (Supporting Information, Section 1.3), it is possible that tunneling through pristine portions of the graphene can occur. However, prior to transport across the graphene, protons need to be desolvated, as evidenced from the lack of OH anion-adsorption features in the CVs (Figure 1).

As the defect density increases, both the H_{UPD}[51] and HER rates increase correspondingly. Therefore, the rate at which protons transport through defects in the graphene must be much higher than that of proton tunneling through pristine graphene. We further envision that there will be a critical defect size where the underlying Pt(111) will start evolving hydrogen like bare Pt(111). When this occurs, the HER rate normalized per geometric area is expected to slightly decrease and asymptotically approach the bare Pt(111) HER rate with increasing defect size (if all graphene eventually delaminates after infinite HER reaction time).

As mentioned in the introduction, the groups of Bao and Zhang demonstrated using DFT computations that the presence of graphene overlayers on a number of substrates (including Pt(111)) and adsorbates (including H) weakens the free energy of adsorption.[6,7,20,21] The CVs of Pt(111) and G/Pt(111) in Figures 1 and 2 also support this computational result since more negative potentials are necessary to adsorb

https://doi.org/10.1021/acscatal.1c02145
ACS Catal. 2021, 11, 10892−10901

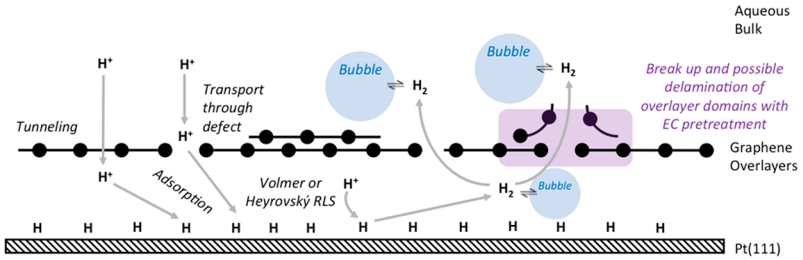

Figure 8. Molecular View of HER on G/Pt(111).

and desorb H in the H_{UPD} region on G/Pt(111) compared to unmodified Pt(111). Since some theoretical studies predict that Pt(111) binds H too strongly for optimal HER kinetics, this weaker binding energy on G/Pt(111) should then lead to improved HER kinetics. If true, this fundamental discovery would demonstrate the promise of confinement modifications in designing catalysts with properties closer to achieving optimum activity while concurrently restricting anions from reaching the underlying metal.

It should be noted that even though this explanation could explain the increase in HER activity after addition of graphene overlayers on Pt(111), it does not rule out the possibility of other explanations such as the influence of electronic effects, structural effects, electrolyte effects, bubble effects, or impurity effects, as further discussed in the Supporting Information Section 5, especially because the observed experimental effects are small, in principle too small to be predicted reliably by DFT. A perhaps more meaningful observation from this work is that to exploit the potential positive effects of G/Pt(111) for HER, the graphene layer needs to be sufficiently defective so as to not hamper H^+ transport across the layer.

3.6. Conclusions. Figure 8 summarizes the molecular picture of HER on G/Pt(111) pieced together from our CV, SEM, and kinetic results. First, H^+ from the bulk electrolyte transports through domain boundaries and defects in the graphene, H^+ undergoes an electron transfer event with Pt(111) to form adsorbed H, and then H^+ reacts with another H or H^+ form H_2. The H_2 then transports through graphene into the electrolyte, and if bubbles are formed, may break up or delaminate graphene overlayers.

In this contribution, we demonstrated that defective graphene overlayers on Pt(111) are necessary to measure kinetically limited HER rates free of transport limitations. These kinetically limited HER rates indicated that the presence of defective graphene overlayers results in HER rates up to 200% faster than on bare Pt(111) while exhibiting indistinguishable Tafel slopes and $[H^+]$ reactant orders. Additionally, graphene overlayers are selective to H^+ and prevent anions (e.g., SO_4^{2-}) from reaching the underlying Pt(111). Furthermore, EC-treated and as-prepared G/Pt(111) are proposed to exhibit different responses toward graphene defect formation. As-prepared G/Pt(111) exhibits initially slower graphene defect formation with HER reaction but with a sudden increase in the anion charge per Pt after about 10 h of HER. EC-treated graphene, on the other hand, exhibits faster graphene defect formation with HER reaction time without the sudden increase in the anion charge per Pt at 10 h of HER. Significantly, we have shown the G/Pt(111) may be a better catalyst for HER than bare Pt(111), but only if the graphene is sufficiently defective so that transport of H^+ across the graphene is not rate limiting.

■ ASSOCIATED CONTENT

Supporting Information

The Supporting Information is available free of charge at https://pubs.acs.org/doi/10.1021/acscatal.1c02145.

Impurities in Chemicals and Back-of-the-Envelope Calculations (Section 1); Benchmarking with the Literature and Validation Tests (Section 2); Electrochemical Measurements (Section 3); Error Propagation Equations for Calculating the Uncertainty (Section 4); Possible explanations for the higher HER rate on G/Pt(111) than Pt(111) (Section 5); Imaging Results (Section 6); References (Section 7) (PDF)

■ AUTHOR INFORMATION

Corresponding Authors

Arthur J. Shih − *Leiden Institute of Chemistry, Leiden University, 2300 RA Leiden, The Netherlands*; Email: a.j.shih@lic.leidenuniv.nl

Marc T. M. Koper − *Leiden Institute of Chemistry, Leiden University, 2300 RA Leiden, The Netherlands*; orcid.org/0000-0001-6777-4594; Email: m.koper@chem.leidenuniv.nl

Author

Nakkiran Arulmozhi − *Leiden Institute of Chemistry, Leiden University, 2300 RA Leiden, The Netherlands*

Complete contact information is available at: https://pubs.acs.org/10.1021/acscatal.1c02145

Author Contributions

‡A.J.S. and N.A. contributed equally to this work.

Notes

The authors declare no competing financial interest.

■ ACKNOWLEDGMENTS

The author acknowledges Marcel Rost for discussions and Ayşe Eren for quantitative SEM analysis.

■ REFERENCES

(1) Medford, A. J.; Vojvodic, A.; Hummelshøj, J. S.; Voss, J.; Abild-Pedersen, F.; Studt, F.; Bligaard, T.; Nilsson, A.; Nørskov, J. K. From the Sabatier Principle to a Predictive Theory of Transition-Metal Heterogeneous Catalysis. *J. Catal.* **2015**, *328*, 36−42.

(2) Trasatti, S. Work Function, Electronegativity, and Electrochemical Behaviour of Metals. III. Electrolytic Hydrogen Evolution in Acid Solutions. *J. Electroanal. Chem. Interfacial Electrochem.* **1972**, *39*, 163−184.

(3) Greeley, J.; Jaramillo, T. F.; Bonde, J.; Chorkendorff, I.; Nørskov, J. K. Computational High-Throughput Screening of Electrocatalytic Materials for Hydrogen Evolution. *Nat. Mater.* **2006**, *5*, 909−913.

(4) Abild-Pedersen, F.; Greeley, J.; Studt, F.; Rossmeisl, J.; Munter, T. R.; Moses, P. G.; Skulason, E.; Bligaard, T.; Nørskov, J. K. Scaling Properties of Adsorption Energies for Hydrogen-Containing Molecules on Transition-Metal Surfaces. *Phys. Rev. Lett.* **2007**, *99*, No. 016105.
(5) Vojvodic, A.; Nørskov, J. K. New Design Paradigm for Heterogeneous Catalysts. *Natl. Sci. Rev.* **2015**, *2*, 140−143.
(6) Zhang, Y.; Weng, X.; Li, H.; Li, H.; Wei, M.; Xiao, J.; Liu, Z.; Chen, M.; Fu, Q.; Bao, X. Hexagonal Boron Nitride Cover on Pt(111): A New Route to Tune Molecule-Metal Interaction and Metal-Catalyzed Reactions. *Nano Lett.* **2015**, *15*, 3616−3623.
(7) Yao, Y.; Fu, Q.; Zhang, Y. Y.; Weng, X.; Li, H.; Chen, M.; Jin, L.; Dong, A.; Mu, R.; Jiang, P.; Liu, L.; Bluhm, H.; Liu, Z.; Zhang, S. B.; Bao, X. Graphene Cover-Promoted Metal-Catalyzed Reactions. *Proc. Natl. Acad. Sci. U.S.A.* **2014**, *111*, 17023−17028.
(8) Sun, M.; Fu, Q.; Gao, L.; Zheng, Y.; Li, Y.; Chen, M.; Bao, X. Catalysis under Shell: Improved CO Oxidation Reaction Confined in Pt@h-BN Core−Shell Nanoreactors. *Nano Res.* **2017**, *10*, 1403−1412.
(9) Thiele, E. W. Relation between Catalytic Activity and Size of Particle. *Ind. Eng. Chem.* **1939**, *31*, 916−920.
(10) Satterfield, C. N. *Mass Transfer in Heterogeneous Catalysis*; The MIT Press, 1970.
(11) Fogler, H. S. *Essentials of Chemical Reaction Engineering*; Pearson Education, 2010.
(12) Hahn, C.; Jaramillo, T. F. Using Microenvironments to Control Reactivity in CO_2 Electrocatalysis. *Joule* **2020**, *4*, 292−294.
(13) Li, F.; Thevenon, A.; Rosas-Hernández, A.; Wang, Z.; Li, Y.; Gabardo, C. M.; Ozden, A.; Dinh, C. T.; Li, J.; Wang, Y.; Edwards, J. P.; Xu, Y.; McCallum, C.; Tao, L.; Liang, Z. Q.; Luo, M.; Wang, X.; Li, H.; O'Brien, C. P.; Tan, C. S.; Nam, D. H.; Quintero-Bermudez, R.; Zhuang, T. T.; Li, Y. C.; Han, Z.; Britt, R. D.; Sinton, D.; Agapie, T.; Peters, J. C.; Sargent, E. H. Molecular Tuning of CO_2-to-Ethylene Conversion. *Nature* **2020**, *577*, 509−513.
(14) Chen, X.; Lin, Z. Z.; Ju, M.; Guo, L. X. Confined Electrochemical Catalysis under Cover: Enhanced CO_2 Reduction at the Interface between Graphdiyne and Cu Surface. *Appl. Surf. Sci.* **2019**, *479*, 685−692.
(15) Intikhab, S.; Rebollar, L.; Li, Y.; Pai, R.; Kalra, V.; Tang, M. H.; Snyder, J. D. Caffeinated Interfaces Enhance Alkaline Hydrogen Electrocatalysis. *ACS Catal.* **2020**, *10*, 6798−6802.
(16) Labrador, N. Y.; Songcuan, E. L.; De Silva, C.; Chen, H.; Kurdziel, S. J.; Ramachandran, R. K.; Detavernier, C.; Esposito, D. V. Hydrogen Evolution at the Buried Interface between Pt Thin Films and Silicon Oxide Nanomembranes. *ACS Catal.* **2018**, *8*, 1767−1778.
(17) Esposito, D. V. Membrane-Coated Electrocatalysts - An Alternative Approach to Achieving Stable and Tunable Electrocatalysis. *ACS Catal.* **2018**, *8*, 457−465.
(18) Beatty, M. E. S.; Gillette, E. I.; Haley, A. T.; Esposito, D. V. Controlling the Relative Fluxes of Protons and Oxygen to Electrocatalytic Buried Interfaces with Tunable Silicon Oxide Overlayers. *ACS Appl. Energy Mater.* **2020**, *3*, 12338−12350.
(19) Gao, M.; Pan, Y.; Huang, L.; Hu, H.; Zhang, L. Z.; Guo, H. M.; Du, S. X.; Gao, H. J. Epitaxial Growth and Structural Property of Graphene on Pt(111). *Appl. Phys. Lett.* **2011**, *98*, No. 033101.
(20) Li, H.; Xiao, J.; Fu, Q.; Bao, X. Confined Catalysis under Two-Dimensional Materials. *Proc. Natl. Acad. Sci. U.S.A.* **2017**, *114*, 5930−5934.
(21) Zhou, Y.; Chen, W.; Cui, P.; Zeng, J.; Lin, Z.; Kaxiras, E.; Zhang, Z. Enhancing the Hydrogen Activation Reactivity of Nonprecious Metal Substrates via Confined Catalysis Underneath Graphene. *Nano Lett.* **2016**, *16*, 6058−6063.
(22) Nørskov, J. K.; Bligaard, T.; Logadottir, A.; Kitchin, J. R.; Chen, J. G.; Pandelov, S.; Stimming, U. Trends in the Exchange Current for Hydrogen Evolution. *J. Electrochem. Soc.* **2005**, *152*, 126−129.
(23) Greeley, J.; Nørskov, J. K.; Kibler, L. A.; El-Aziz, A. M.; Kolb, D. M. Hydrogen Evolution over Bimetallic Systems: Understanding the Trends. *ChemPhysChem* **2006**, *7*, 1032−1035.
(24) Fu, Y.; Rudnev, A. V.; Wiberg, G. K. H.; Arenz, M. Single Graphene Layer on Pt(111) Creates Confined Electrochemical Environment via Selective Ion Transport. *Angew. Chem., Int. Ed.* **2017**, *56*, 12883−12887.
(25) Baby, A.; Perilli, D.; Liu, H.; Kosmala, T.; Granozzi, G.; Agnoli, S.; Di Valentin, C. In *Tuning the Hydrogen Evolution Reaction at the Pt(111) Surface with Graphene and Non-Precious Metal*, Graphene 2DM Online Conference (GO2020), October 19, 2020.
(26) Baby, A.; Trovato, L.; Di Valentin, C. Single Atom Catalysts (SAC) Trapped in Defective and Nitrogen-Doped Graphene Supported on Metal Substrates. *Carbon* **2021**, *174*, 772−788.
(27) Hu, K.; Ohto, T.; Nagata, Y.; Wakisaka, M.; Aoki, Y.; Fujita, J.; Ito, Y. Catalytic Activity of Graphene-Covered Non-Noble Metals Governed by Proton Penetration in Electrochemical Hydrogen Evolution Reaction. *Nat. Commun.* **2021**, *12*, No. 203.
(28) Bunch, J. S.; Verbridge, S. S.; Alden, J. S.; van der Zande, A. M.; Parpia, J. M.; Craighead, H. G.; McEuen, P. L. Impermeable Atomic Membranes from Graphene Sheets. *Nano Lett.* **2008**, *8*, 2458−2462.
(29) Hu, S.; Lozada-Hidalgo, M.; Wang, F. C.; Mishchenko, A.; Schedin, F.; Nair, R. R.; Hill, E. W.; Boukhvalov, D. W.; Katsnelson, M. I.; Dryfe, R. A. W.; Grigorieva, I. V.; Wu, H. A.; Geim, A. K. Proton Transport through One-Atom-Thick Crystals. *Nature* **2014**, *516*, 227−230.
(30) Lozada-Hidalgo, M.; Hu, S.; Marshall, O.; Mishchenko, A.; Grigorenko, A. N.; Dryfe, R. A. W.; Radha, B.; Grigorieva, I. V.; Geim, A. K. Sieving Hydrogen Isotopes through Two-Dimensional Crystals. *Science* **2016**, *351*, 68−70.
(31) Ferrell, R. T.; Himmelblau, D. M. Diffusion Coeffcients of Hydrogen and Helium in Water. *AIChE J.* **1967**, *13*, 702−708.
(32) Sun, P. Z.; Yang, Q.; Kuang, W. J.; Stebunov, Y. V.; Xiong, W. Q.; Yu, J.; Nair, R. R.; Katsnelson, M. I.; Yuan, S. J.; Grigorieva, I. V.; Lozada-Hidalgo, M.; Wang, F. C.; Geim, A. K. Limits on Gas Impermeability of Graphene. *Nature* **2020**, *579*, 229−232.
(33) Dong, G. C.; Van Baarle, D. W.; Rost, M. J.; Frenken, J. W. M. Graphene Formation on Metal Surfaces Investigated by In-Situ Scanning Tunneling Microscopy. *New J. Phys.* **2012**, *14*, No. 053033.
(34) Feng, X.; Maier, S.; Salmeron, M. Water Splits Epitaxial Graphene and Intercalates. *J. Am. Chem. Soc.* **2012**, *134*, 5662−5668.
(35) Dollekamp, E.; Bampoulis, P.; Poelsema, B.; Zandvliet, H. J. W.; Kooij, E. S. Electrochemically Induced Nanobubbles between Graphene and Mica. *Langmuir* **2016**, *32*, 6582−6590.
(36) Yasuda, S.; Tamura, K.; Terasawa, T.; Yano, M.; Nakajima, H.; Morimoto, T.; Okazaki, T.; Agari, R.; Takahashi, Y.; Kato, M.; Yagi, I.; Asaoka, H. Confinement of Hydrogen Molecules at Graphene−Metal Interface by Electrochemical Hydrogen Evolution Reaction. *J. Phys. Chem. C* **2020**, *124*, 5300−5307.
(37) Arulmozhi, N.; Esau, D.; van Drunen, J.; Jerkiewicz, G. Design and Development of Instrumentations for the Preparation of Platinum Single Crystals for Electrochemistry and Electrocatalysis Research Part 3: Final Treatment, Electrochemical Measurements, and Recommended Laboratory Practices. *Electrocatalysis* **2018**, *9*, 113−123.
(38) Clavilier, J.; Faure, R.; Guinet, G.; Durand, R. Preparation of Monocrystalline Pt Microelectrodes and Electrochemical Study of the Plane Surfaces Cut in the Direction of the {111} and {110} Planes. *J. Electroanal. Chem. Interfacial Electrochem.* **1980**, *107*, 205−209.
(39) Kibler, L. A. Preparation and Characterization of Noble Metal Single Crystal Electrode Surfaces Preparation and Characterization of Noble Metal Single Crystal Electrode. *Surfaces. Int. Soc. Electrochem.* **2003**, 1−56.
(40) Vlassiouk, I.; Regmi, M.; Fulvio, P.; Dai, S.; Datskos, P.; Eres, G.; Smirnov, S. Role of Hydrogen in Chemical Vapor Deposition Growth of Large Single-Crystal Graphene. *ACS Nano* **2011**, *5*, 6069−6076.
(41) Radev, I.; Cho, Y.-H.; Koutzarov, K.; Sung, Y.-E.; Tsotridis, G. The Effect of the Geometric Area Ratio between Working and Counter PEM Electrodes for Electrochemical Hydrogen Reactions. *Int. J. Hydrogen Energy* **2010**, *35*, 12449−12453.

https://doi.org/10.1021/acscatal.1c02145
ACS Catal. 2021, 11, 10892−10901

(42) Villullas, H. M.; Lopez Teijelo, M. Meniscus Shape and Lateral Wetting at the Hanging Meniscus Rotating Disc (HMRD) Electrode. *J. Appl. Electrochem.* **1996**, *26*, 353−359.
(43) Ives, D. J. G.; Janz, G. J.; King, C. V. Reference Electrodes: Theory and Practice. *J. Electrochem. Soc.* **1961**, *108*, 246C.
(44) Landis, J. R.; Koch, G. G. The Measurement of Observer Agreement for Categorical Data. *Biometrics* **1977**, *33*, 159−174.
(45) Jost, A. P.-T.; Waters, J. C. Designing a Rigorous Microscopy Experiment: Validating Methods and Avoiding Bias. *J. Cell Biol.* **2019**, *218*, 1452−1466.
(46) Ku, H. H. Notes on the Use of Propagation of Error Formulas. *J. Res. Natl. Bur. Stand., Sect. C* **1966**, *70C*, 263−273.
(47) Karlberg, G. S.; Jaramillo, T. F.; Skúlason, E.; Rossmeisl, J.; Bligaard, T.; Nørskov, J. K. Cyclic Voltammograms for H on Pt(111) and Pt(100) from First Principles. *Phys. Rev. Lett.* **2007**, *99*, 1−4.
(48) Kita, H.; Ye, S.; Gao, Y. Mass Transfer Effect in Hydrogen Evolution Reaction on Pt Single-Crystal Electrodes in Acid Solution. *J. Electroanal. Chem.* **1992**, *334*, 351−357.
(49) Gómez, R.; Fernández-Vega, A.; Feliu, J. M.; Aldaz, A. Hydrogen Evolution on Platinum Single Crystal Surfaces: Effects of Irreversibly Adsorbed Bismuth and Antimony on Hydrogen Adsorption and Evolution on Platinum (100). *J. Phys. Chem. A* **1993**, *97*, 4769−4776.
(50) Marković, N. M.; Grgur, B. N.; Ross, P. N. Temperature-Dependent Hydrogen Electrochemistry on Platinum Low-Index Single-Crystal Surfaces in Acid Solutions. *J. Phys. Chem. B* **1997**, *101*, 5405−5413.
(51) Arulmozhi, N.; Tudor, V.; Chen, X.; van Velden, D.; Schneider, G. F.; Koper, M. T. M. Electroadsorption under Cover: The Nature of Hydrogen Adsorption onto Graphene Covered Pt(111) Electrode. *Prep.* **2021**.
(52) Ferrari, A. G.-M.; Brownson, D. A. C.; Banks, C. E. Investigating the Integrity of Graphene towards the Electrochemical Hydrogen Evolution Reaction (HER). *Sci. Rep.* **2019**, *9*, No. 15961.
(53) Bard, A. J.; Faulkner, L. R. *Electrochemical Methods: Fundamentals and Applications*, 2nd ed.; Wiley, 2001.
(54) Zalitis, C. M.; Kucernak, A. R.; Sharman, J.; Wright, E. Design Principles for Platinum Nanoparticles Catalysing Electrochemical Hydrogen Evolution and Oxidation Reactions: Edges Are Much More Active than Facets. *J. Mater. Chem. A* **2017**, *5*, 23328−23338.
(55) Koper, M. T. M.; Lukkien, J. J. Modeling the Butterfly: The Voltammetry of $(\sqrt{3}\times\sqrt{3})$R30° and p(2×2) Overlayers on (111) Electrodes. *J. Electroanal. Chem.* **2000**, *485*, 161−165.
(56) Koper, M. T. M.; Lukkien, J. J. Modeling the Butterfly: Influence of Lateral Interactions and Adsorption Geometry on the Voltammetry at (111) and (100) Electrodes. *Surf. Sci.* **2002**, *498*, 105−115.
(57) Foiles, S. M.; Baskes, M. I.; Daw, M. S. Embedded-Atom-Method Functions for the Fcc Metals Cu, Ag, Au, Ni, Pd, Pt, and Their Alloys. *Phys. Rev. B* **1986**, *33*, 7983−7991.
(58) Krupski, K.; Moors, M.; Jozwik, P.; Kobiela, T.; Krupski, A. Structure Determination of Au on Pt(111) Surface: LEED, STM and DFT Study. *Materials* **2015**, *8*, 2935−2952.
(59) Perrin, J. Mouvement Brownien et Grandeurs Moléculaires. *Radium* **1909**, *6*, 353−360.
(60) Avogadro, A. Essai d'une Manière de Déterminer Les Masses Relatives Des Molécules Élémentaires Des Corps, et Les Proportions Selon Lesquelles Elles Entrent Dans Les Combinaisons. *J. Phys. Chim. d'histoire Nat. des arts* **1811**, *73*, 58−76.
(61) Yu, S. U.; Park, B.; Cho, Y.; Hyun, S.; Kim, J. K.; Kim, K. S. Simultaneous Visualization of Graphene Grain Boundaries and Wrinkles with Structural Information by Gold Deposition. *ACS Nano* **2014**, *8*, 8662−8668.
(62) Zaretski, A. V.; Lipomi, D. J. Processes for Non-Destructive Transfer of Graphene: Widening the Bottleneck for Industrial Scale Production. *Nanoscale* **2015**, *7*, 9963−9969.
(63) Stolyarova, E.; Stolyarov, D.; Bolotin, K.; Ryu, S.; Liu, L.; Rim, K. T.; Klima, M.; Hybertsen, M.; Pogorelsky, L.; Pavlishin, L.; Kusche, K.; Horie, J.; Kim, P.; Stormer, H. L.; Yakimenko, V.; Flynn, G. Observation of Graphene Bubbles and Effective Mass Transport under Graphene Films. *Nano Lett.* **2009**, *9*, 332−337.
(64) Palacio, I.; Otero-Irurueta, G.; Concepción, A.; Martínez, J. I.; López-Elvira, E.; Muñoz-Ochando, I.; Salavagione, H. J.; López, M. F.; García-Hernández, M.; Méndez, J.; Ellis, G. J.; Martín-Gago, J. A. Chemistry below Graphene: Decoupling Epitaxial Graphene from Metals by Potential-Controlled Electrochemical Oxidation. *Carbon* **2018**, *129*, 837−846.
(65) Yoon, D.; Son, Y. W.; Cheong, H. Negative Thermal Expansion Coefficient of Graphene Measured by Raman Spectroscopy. *Nano Lett.* **2011**, *11*, 3227−3231.
(66) Ferrighi, L.; Perilli, D.; Selli, D.; Valentin, C. Di. Water at the Interface Between Defective Graphene and Cu or Pt (111) Surfaces. *ACS Appl. Mater. Interfaces* **2017**, *9*, 29932−29941.
(67) Zheng, J.; Yan, Y.; Xu, B. Correcting the Hydrogen Diffusion Limitation in Rotating Disk Electrode Measurements of Hydrogen Evolution Reaction Kinetics. *J. Electrochem. Soc.* **2015**, *162*, F1470−F1481.
(68) Rheinländer, P. J.; Herranz, J.; Durst, J.; Gasteiger, H. A. Kinetics of the Hydrogen Oxidation/Evolution Reaction on Polycrystalline Platinum in Alkaline Electrolyte Reaction Order with Respect to Hydrogen Pressure. *J. Electrochem. Soc.* **2014**, *161*, F1448−F1457.
(69) Shinagawa, T.; Garcia-Esparza, A. T.; Takanabe, K. Insight on Tafel Slopes from a Microkinetic Analysis of Aqueous Electrocatalysis for Energy Conversion. *Sci. Rep.* **2015**, *5*, No. 13801.
(70) Ledezma-Yanez, I.; Wallace, W. D. Z.; Sebastián-Pascual, P.; Climent, V.; Feliu, J. M.; Koper, M. T. M. Interfacial Water Reorganization as a pH-Dependent Descriptor of the Hydrogen Evolution Rate on Platinum Electrodes. *Nat. Energy* **2017**, *2*, No. 17031.
(71) Ojha, K.; Arulmozhi, N.; Aranzales, D.; Koper, M. T. M. Double Layer at the Pt(111)−Aqueous Electrolyte Interface: Potential of Zero Charge and Anomalous Gouy−Chapman Screening. *Angew. Chem., Int. Ed.* **2020**, *59*, 711−715.
(72) Bohra, D.; Chaudhry, J. H.; Burdyny, T.; Pidko, E. A.; Smith, W. A. Modeling the Electrical Double Layer to Understand the Reaction Environment in a CO_2 Electrocatalytic System. *Energy Environ. Sci.* **2019**, *12*, 3380−3389.

https://doi.org/10.1021/acscatal.1c02145
ACS Catal. 2021, 11, 10892−10901